Estimating distances to tipping points from dryland ecosystem images

Benoît Pichon[1,*] (Orcid: 0009-0007-6206-5482)

Sophie Donnet[2] (Orcid: 0000-0003-4370-7316)

Isabelle Gounand[3] (Orcid: 0000-0002-0675-3973)

Sonia Kéfi[1,4] (Orcid: 0000-0002-9678-7770)

1. ISEM, Univ Montpellier, CNRS, EPHE, IRD, F-34095 Montpellier, France;

2. UMR MIA-Paris, AgroParisTech, INRA, Université Paris-Saclay, 75005, Paris, France;

3. Institut d'écologie et des sciences de l'environnement (iEES Paris), Sorbonne Université, CNRS, UPEC, CNRS, IRD, INRA, 75005 Paris, France.

4. Santa Fe Institute, 1399 Hyde Park Road, Santa Fe, NM 87501, USA

∗ Corresponding authors; *benoit.pichon0@gmail.com*

Data: The code and the data are available on GitHub via Zenodo: 10.5281/zenodo.10672395

Abstract

Resource-limited environments, such as drylands, can exhibit self-organized spatial patterns. Theory suggests that these patterns could be indicators of approaching tipping points towards ecosystem degradation. However, we still lack ways of estimating a distance to tipping points that is comparable across sites. Here, we present a model-driven approach to do just that in self-organized ecosystems based on images. After validating the approach on simulated data, we applied it to a global dryland dataset, placed sites along a vulnerability gradient and studied the drivers of the estimated distance to tipping points. Crossing this distance with the sites' aridity projections made it possible to pinpoint the most fragile sites among those studied. Our approach paves the way for a general risk assessment method for spatially self-organized ecosystems.

Introduction

The dynamics of complex systems are knowingly difficult to predict. Examples from past societies (Centeno et al., 2023), climatic (Lenton et al., 2008), or financial (Battiston et al., 2016) systems emphasize that some complex systems can undergo rapid and unexpected collapses, hereafter also referred to as 'tipping points'. In ecology, there are evidence from such rapid shifts in drylands, savannas, or coral-reefs for example, where abrupt changes in species composition and ecosystem functioning can occur with important ecological and social consequences (Kéfi et al., 2007a; Mumby et al., 2007; Scheffer, 2009).

Because these shifts are often unexpected, previous research has been devoted to the search for indicators of their approach. Generic 'early warning signals', such as temporal autocorrelation and variance, have been developed in theoretical models (Scheffer et al., 2009) and quantified on time series data from a variety of systems, including financial or societal crisis (Battiston et al., 2016), emotion fluctuations in humans (Van De Leemput et al., 2014) and changes in ecosystem states (e.g., (Carpenter et al., 2011; Veraart et al., 2012; van Belzen et al., 2017)). These temporal early warning signals, however, require long time series and can fail in a number of contexts (Hastings & Wysham, 2010; Boettiger & Hastings, 2013; Burthe et al., 2016), including in strongly spatially-structured ecosystems (Dakos et al., 2011).

In addition to exhibiting shifts, a number of ecosystems, such as drylands, mussel-beds, and salt marshes, also have a characteristic spatial structure (Aguiar & Sala, 1999; Guichard et al., 2003; van der Heide et al., 2010). In these resource-limited environments, interactions between species and their local environment generate positive feedback loops that enhance the local environmental conditions and buffer species against disturbances (Aguiar & Sala, 1999; Guichard et al., 2003; van der Heide et al., 2010; Berdugo et al., 2017). Such facilitation mechanisms, which are known to underly catastrophic shifts, generate an emergent spatial structure, referred to as 'self-organized', with patches of individuals aggregated in space interspersed by open areas (Rietkerk et al., 2002; van de Koppel et al., 2008; Kéfi et al.,

2024).

These spatial patterns can be reproduced by dynamical models (Rietkerk et al., 2002; Kéfi et al., 2007b; Manor & Shnerb, 2008; Kéfi et al., 2011). In these models, when conditions become harsher, predictable changes in spatial structure are observed until the collapse of the system. Studies suggested that spatial structure could hence be used as indicator of resilience in self-organized ecosystems (Kéfi et al., 2011, 2014; van Belzen et al., 2017).

While these spatial indicators of resilience provide a promising way of diagnosing the loss of resilience of a given system approaching its tipping point, there is in practice not a single spatial metric available in the literature but a collection of them ; this means that, when considered jointly, some of them may sometimes provide conflicting information, and it is not obvious how to combine them into a single indicator (Kéfi et al., 2014; Eby et al., 2017). Furthermore, those metrics do not provide an actual distance to tipping point that is comparable in sites characterized by, for example, different vegetation, environmental, or soil conditions. Operationalizing these indicators to identify the most fragile ecosystems requires overcoming these limitations and finding a way of estimating a distance to a tipping point in a way that is comparable across field sites that differ in many ways (Zhang et al., 2022).

Estimating distances to tipping point

Here, we propose to tackle these limitations using an inverse approach that directly estimates the distance to tipping point from the observed spatial structure of ecosystems. The approach relies on a minimal, identifiable model which is able to generate the spatial structure typical of various self-organized ecosystems and their changes along gradients (Methods). Our model relies on two parameters, namely p that quantifies the net recruitment of occupied sites (*e.g.* by vegetation) and q a spatial aggregation parameter

related to the facilitation strength, which generates the emergent spatial structure. In order to infer these parameters from observations, we enhance this minimal model with an observational layer used to match the scales of the processes in the ecological model and in the observations (Methods). We estimate the parameters of that model from observed spatially structured landscapes using Approximate Bayesian Computing (ABC): we generate a large number of simulated landscapes from the model, compare each observed landscape to simulated ones through a discrepancy measure based on the spatial structure, and retrieve a sample of parameters (p_{est}, q_{est}), leading to simulated landscapes whose spatial structures are the most similar to each observed landscape (Fig. 1A).

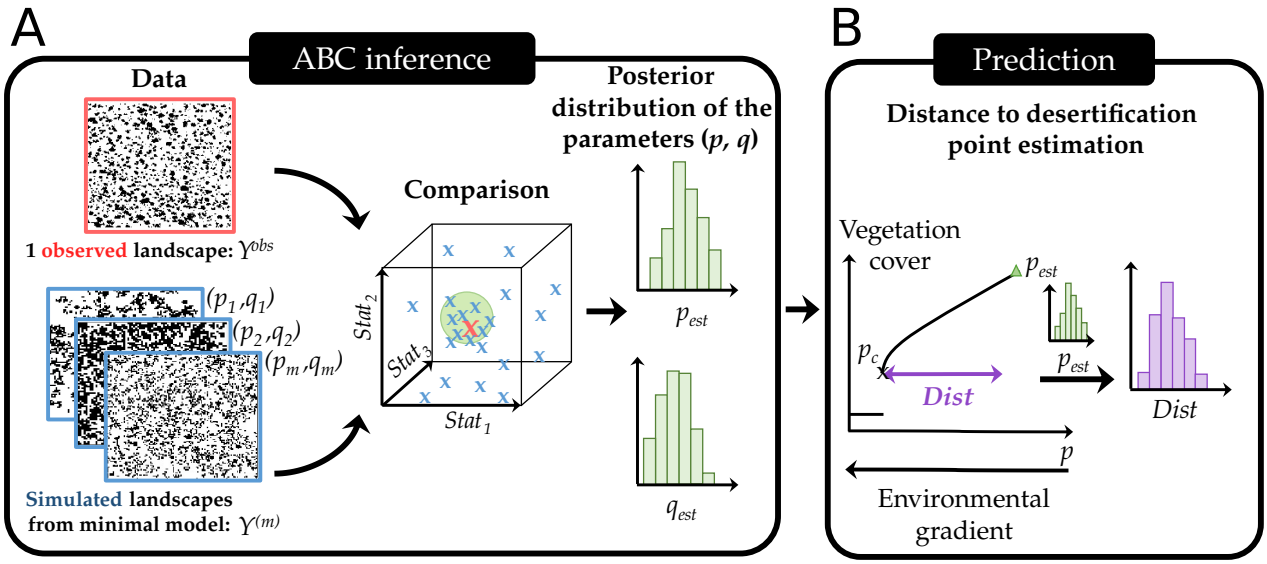

Figure 1: **Overview of the inference approach to estimate distance to tipping point from spatially structured ecosystem images.**
The approach uses a simple mechanistic model (the so-called minimal model) and Approximate Bayesian Computing inference method to estimate parameters generating realistic spatial structures and derive distance to the tipping point for spatially structured ecosystems. (A) We linked observed (bottom row) and simulated (top row) vegetation landscapes using an inference approach (Methods) that allows estimating a distribution of the parameters of the minimal model ($(p_{\text{est}}, q_{\text{est}})$). (B) Using the estimated parameters $(p_{\text{est}}, q_{\text{est}})$, we simulated a scenario of increasing abiotic stress and derived the distance to the desertification point in the minimal model.

Finally, for each observed landscape, once we know its current state through its estimated p_{est} and q_{est}, we mimic a scenario of increasing stress by simulating the minimal

model with a decreasing probability of recruitment p until the tipping point p_c (Fig. 1B). This prediction procedure thereby allows recovering the distance to a tipping point along the p-axis ($p_{est} - p_c$; Methods).

Validating the approach on simulations

To test the robustness of the minimal model, we evaluated it on simulated landscapes from two models with different mechanisms than those of the minimal model but exhibiting similar emergent spatial patterns (Fig. S1). We used a dryland vegetation model with more complex description of plant life history traits (seven parameters capturing dispersal, facilitation, recruitment, competition) (Kéfi et al., 2007b) and a model from a different type of ecosystem, namely a mussel-bed model containing three parameters (Guichard et al., 2003) (Fig. 2A; Methods). Simulations from these two models generated a bank of observed spatial landscapes, for which the actual distance to the tipping point is numerically assessed. We then performed the approach on each of these landscapes and inferred a distance to the tipping point using the minimal model (Fig. 2B). We then compared this inferred distance to the 'real' one calculated in the two original models used to generate the landscapes (Fig. 2C).

We found that the minimal model successfully reproduces spatial patterns generated using either the vegetation or the mussel-bed model (Figs. 2B, supplementary text). Importantly, the approach reliably ranks landscapes along an axis corresponding to the distance to the tipping point (median Spearman correlation = 0.98 and 0.9 for the dryland and mussel-bed models respectively; Figs. 2C and see S2, S3 for extensive parameter sets).

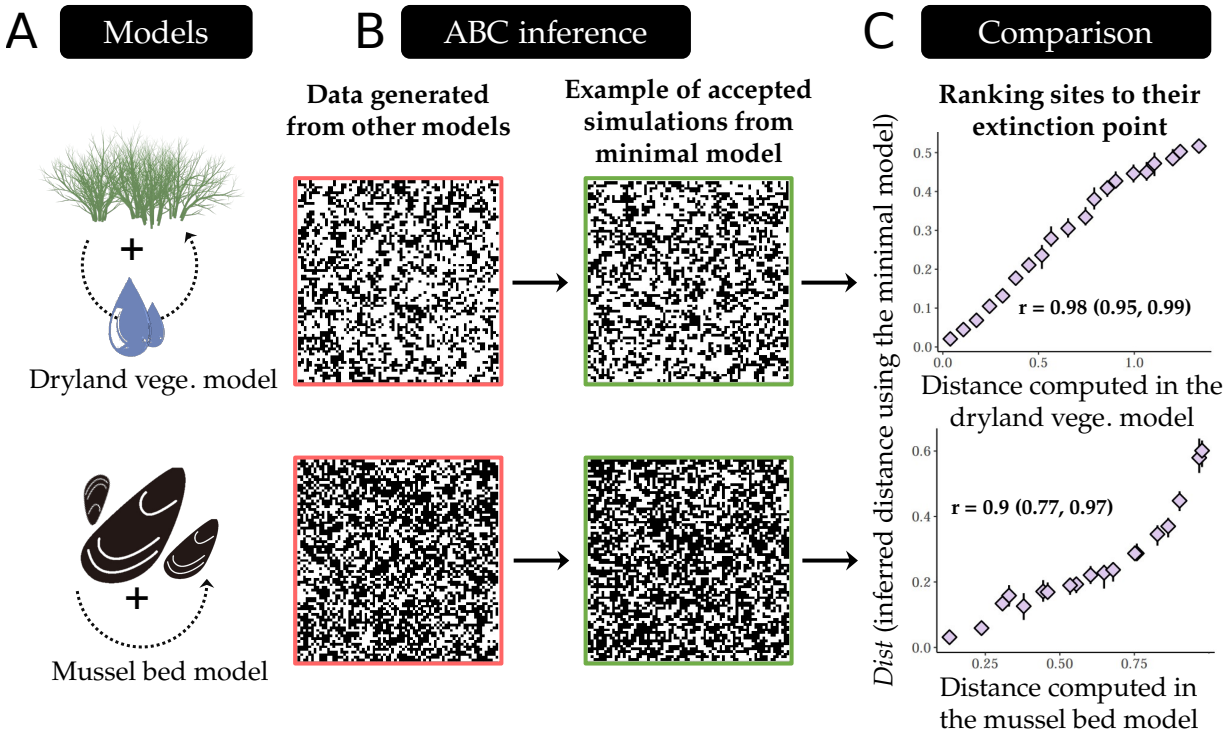

Figure 2: **Validating the minimal model choice and inference approach using simulations.**
(A,B) We used a dryland vegetation model and a mussel-bed model that generate self-organized irregular patterns, and we performed the inference approach on landscapes generated by these models. (C) Then, we compared the distance to the extinction state computed in the two models (x-axis) to those estimated using our approach (y-axis). Spearman correlation is displayed on the panels with its confidence intervals. See Figs. S2, S3 for a more extensive validation.

Application to drylands

We next applied the approach to a global dryland data set corresponding to 293 images from 115 sites located around the globe, on which soil and vegetation attributes were measured (Maestre et al., 2012; Berdugo et al., 2017). This allowed estimating the distance to the tipping point (here to the desertified state) for each of these images, making it possible to place each dryland image on a quantitative axis corresponding to a distance to the desertification point, and thereby providing an estimation of their resilience to upcoming perturbations (Fig. S4, and see as an example, the three sites in Fig. S5).

As intuitively expected, we find that sites with a higher vegetation cover tend to be farther away from their desertification point (Fig. S6). On the contrary, sites with a higher spatial autocorrelation of vegetation (Moran I) tend to be closer to the desertification point (Fig. S7A). Importantly, we also find that their joint-information is needed to accurately estimate the distance to the desertification point (Fig. S8).

We then investigated how local drivers affect directly and indirectly each of the three following response variables (Fig. 3): the distance to the desertification point, vegetation cover and the spatial autocorrelation of vegetation (Moran I). The local drivers considered are the aridity level (1-precipitation/potential evapotranspiration), a multifunctionality index quantifying the functioning of sites as the Z-score of 16 soil variables related to carbon, nitrogen and phosphorus cycling and storage, and the plant facilitation strength that is available for a subset of 70 of the 115 sites (Methods). To get a better overview of the dependencies, we plugged the vegetation cover, the Moran I and the local drivers into a structural equation model to disentangle relationships and account for compensatory effects between drivers (Methods).

We found that sites with higher levels of soil multifunctionality are characterized by higher vegetation cover and spatial autocorrelation of their vegetation (Fig. 3D). This suggests that drylands' spatial structure is a good predictor of their functioning (and conversely), consistently with (Aguiar & Sala, 1999; Berdugo et al., 2017; Kéfi et al.,

2024). Because the vegetation cover and the spatial autocorrelation of the vegetation have opposite effects on the distance to the desertification point (Fig. 3D), soil multifunctionality is found to be weakly positively associated with the distance to the desertification point, meaning that sites farther away from their desertification point tend to show slightly higher functioning (Fig. 3A). By estimating a comparable distance to the desertification point across drylands, these results contribute to showing that the positive feedback between vegetation cover and ecosystem functioning may contribute to increasing drylands' resilience (Kéfi et al., 2024).

For a subset of sites on which the level of plant facilitation was measured in the field ($n = 70$ sites; Methods), we observe a negative association between facilitation and soil multifunctionality (Fig. S9) and a weak negative association between the level of facilitation and the distance to the desertification point, meaning that sites closer to their desertification point tend to show higher levels of facilitation despite a lower soil multifunctionality (Fig. 3D). This echoes the stress-gradient hypothesis, which suggests that facilitation increases with higher abiotic stress on ecosystems (He et al., 2013). Theoretical models show that higher levels of facilitation in plant communities can lead to a higher vegetation cover and the maintenance of the vegetation for higher stress levels than communities without facilitation (Kéfi et al., 2007b; Koffel et al., 2021). By allowing species to extend their abiotic niche, facilitation contributes to buffer the effects of abiotic pressure on drylands' functioning and resilience (e.g. (Danet et al., 2021)). However, facilitation has also been shown to lead to possible abrupt transitions to desertified landscapes because facilitation contributes to positive feedback loops (Kéfi et al., 2016). So, as the stress level increases and communities approach their desertification point, if facilitation is increasing as we observe in our results, facilitation might maintain a relatively high cover all along the gradient, but then collapse more abruptly (from a higher vegetation cover) when communities reach their tipping point.

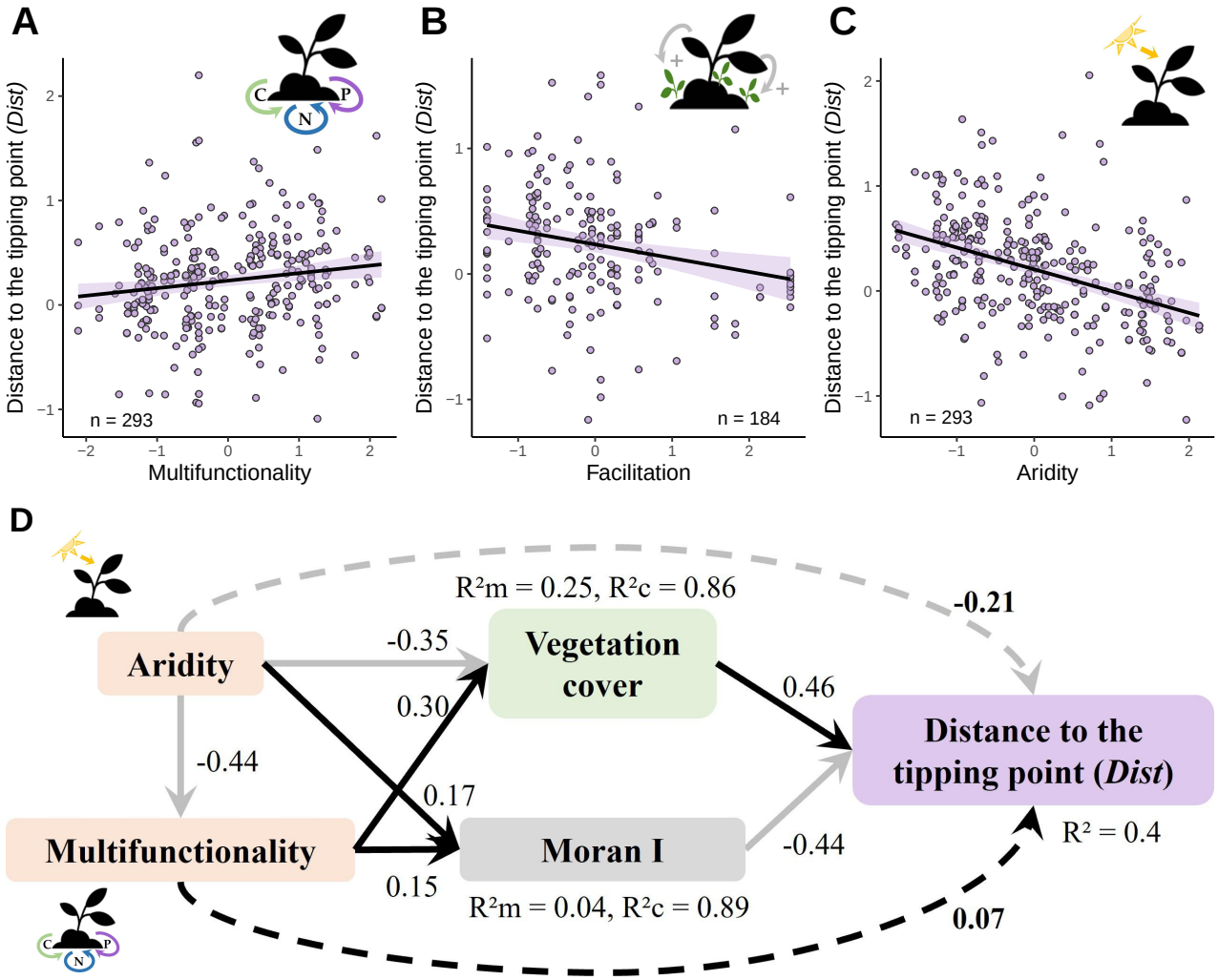

Figure 3: **Estimating distances to the desertification points across global drylands.** (A-C) Predicted responses of the distance of the desertification point (*Dist*) to changes in multifunctionality (A), facilitation strength (B), and aridity (C). The points show partial residuals, and the lines correspond to model fits. Shading around each line represents the 95% confidence interval. All slopes were significantly different from 0. Model fits are available in Table S1 and models R^2 are available in Table S3. (D) Structural equation model decomposing the effects of aridity and multifunctionality on the vegetation cover, aggregation of the vegetation (Moran I) and the distance to the desertification point. Direct effects correspond to full lines, while indirect ones correspond to dashed ones. Facilitation was not included in the SEM since it was only measured for 70 sites among the 115 ones (184 landscapes). SEM: n = 293 landscapes, Goodness of fit: Fisher C stat = 1.584, degrees of freedom=2, *P*-value = 0.812. SEM coefficients confidence intervals are located in Table S2.

Last, we show that sites experiencing higher aridity levels tend to have lower vegetation cover, which results in a negative association between aridity and distance to the desertification point (Fig. 3C). The negative indirect effect of aridity on the resilience of sites is further mediated by the functioning of sites, since high aridity levels are associated with lower nutrient and carbon cycling (Fig. 3D). Given that drylands are experiencing increasing aridity levels (Huang et al., 2016), these changes will likely push drylands toward their desertification point, as it is already observed in some areas (Burrell et al., 2020).

Drylands cover 41% of the land surface and host more than 2 billion people (Reynolds et al., 2007). There is thereby a need to build knowledge on these ecosystems and understand their possible responses to increasing levels of perturbations. We provide the first approach that allows quantifying a comparable distance to a tipping point for spatially-structured ecosystems. Compared to other studies that investigate how spatial indicators change along environmental gradients (Eby et al., 2017; van Belzen et al., 2017; Majumder et al., 2019; Buxton et al., 2022), our approach allows to quantitatively rank sites along a vulnerability axis defined as the distance to a desertification point. Because the method only relies on a snapshot of an ecosystem, and not on large spatio-temporal data, it opens new avenues to develop methods aiming at globally monitoring ecosystems using spatial data (Deblauwe et al., 2008; Lenton et al., 2022). Beyond drylands, our approach could also be applied to other ecosystems. In fact, the minimal model we used can be relevant for other systems where entities aggregate in space because they are involved in local positive feedbacks that generate a characteristic irregular two-phase spatial structure (Supplementary text). In intertidal systems for example, both mussels and sea-grasses perform facilitation, which promotes the emergence of spatial patterning of sea-grasses and mussels (Guichard et al., 2003; Maxwell et al., 2017). When applied to a theoretical model of mussel-beds, our framework indeed proved to successfully predict the resilience of intertidal ecosystems from their emergent spatial structure (Figs. 2, S3). Given the increasing availability of ecosystem images, further efforts in the direction of quantifying

resilience could allow building a toolbox to estimate distances to tipping points in many systems (Zhang et al., 2022).

It is noteworthy that our approach here relies on estimating the distance to tipping point using the parameter p of our minimal model, assumed to mimic aridity. This is a step forward to currently available tools used to estimate ecosystem resilience, especially because it allows comparing the resilience of different sites (and not how the resilience of a given site evolves through time). However, future research should also investigate the extent to which this approach predicts well changes in other types of pressures such as grazing, which can have a spatial component (Schneider & Kéfi, 2016). Additionally, it is important to note that we still lack metrics that can be interpreted as a timescale or a distance in driver-scale, such as the exact amount of change in aridity level that would lead to the collapse of a given ecological site. The use of long term data-sets (Lu et al., 2022) or historical images (Barbier et al., 2006; Deblauwe et al., 2012) could help getting a better sense for the characteristic timescale of changes in drylands.

Identifying the most fragile sites

In sum, we believe that our approach can provide operational information to pinpoint the most fragile dryland areas based on images. We illustrate possible applications of our approach by crossing our resilience estimations with aridity projection using the IPCC's (Intergovernmental Panel on Climate Change) scenario assuming a sustained increase in carbon emission (i.e. scenario RCP 8.5). We categorized the 293 landscapes into five vulnerability groups based on cluster analysis (Methods). Among these groups, 'high risk' landscapes (red points in Fig. 4) are both relatively close to their desertification point and expected to undergo a rapid increase in aridity in the next decades. Some landscapes are projected to experience similar changes in aridity, but are further away from their desertification point, and therefore classified as under 'climatic risk' (orange

and yellow points in Fig. 4). These landscapes typically have a higher vegetation cover and slightly higher soil multifunctionality compared to the high risk landscapes (Fig. S10). By contrast, landscapes under 'ecological risk' are relatively close to their desertification point while projected to undergo relatively small increase in aridity. These sites are currently characterized by relatively high aridity and facilitation levels compared to the other vulnerability groups (Fig. S10). Compared to the high risk landscapes, we expect the functional composition of these communities to be represented by more stress-tolerant and facilitating plant species (Pichon et al., 2024; Liancourt et al., 2005; Frenette Dussault et al., 2013). These analyses suggest that conservation efforts should prioritize on dryland sites that currently experience low abiotic stress but are expected to undergo rapid changes (i.e. the red and orange points in Fig. 4). Our approach represents a first operational step towards comparing and ranking sites at risk in self-organized ecosystems, and paves the way for reliable prediction of ecosystem resilience to environmental change.

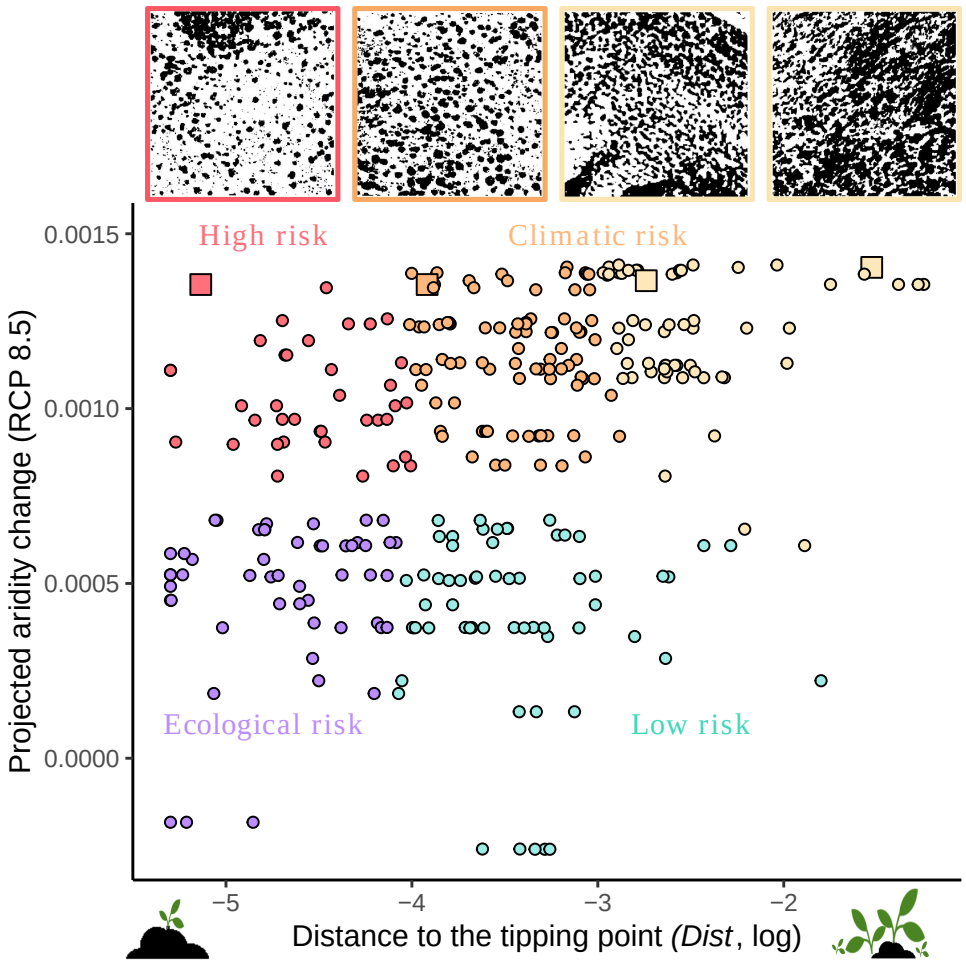

Figure 4: **Crossing estimated distance to the desertification point with aridity projections to pinpoint most vulnerable sites.**
We mapped all sites into a 2D space defined by the distance to the desertification point (*Dist*, x-axis) and the linear trend of aridity for 1950–2100 under the IPCC RCP 8.5 scenario (y-axis). Then, we delimited four vulnerability clusters (”high risk”, ”climatic risk”,”ecological risk”,”low risk”). Red points, for instance, correspond to sites both close to their desertification point and expected to undergo rapid aridity increase in the next decades. The characteristics of the clusters can be found in Fig. S10. Four vegetation landscapes located in Spain and expected to experience a rapid increase in aridity are given as examples. Their point shape is a square and is slightly bigger than the other points to allow their identification.

Materials and Methods

Our overarching aim is to infer the parameters of a minimal model for any observed landscape with irregular patterns, and use the parameters of this fitted model to estimate a distance to a tipping point.

Data: Observed vegetation landscapes

345 images of dryland ecosystems were taken from Berdugo et al., (2017) (Berdugo et al., 2017; Miguel Berdugo et al., 2017). These images, which correspond to 50m $\times$ 50m landscapes, have a resolution sufficient to identify vegetation patches (spatial resolution lower than 0.3 meters per pixel). The 345 images are distributed over 115 geographical locations in 13 countries. The choice of theses geographic locations was guided by the BIOCOM dataset, which gathered different biotic and abiotic conditions on these particular locations (see (Maestre et al., 2012; Berdugo et al., 2017) for details; Fig. S11). For each geographic location, multiple soil attributes were collected: the soil sand content, the so-called multifunctionality index (*i.e.,* a Z-score of 16 soil variables associated with carbon, nitrogen and phosphorous cycling and storage etc.., see (Maestre et al., 2012)), the soil amelioration index, measured as the difference in organic carbon content between vegetated and bare soil areas, and the level of facilitation (*i.e.,* the proportion of plant species that are significantly more in the neighborhood of a facilitating species). To measure the latter, the number of individuals found in open areas is compared to those found under facilitating species (*i.e.,* nurses) and an χ^2 is computed on each pairwise interaction (see (Soliveres et al., 2014; Soliveres & Maestre, 2014) for further details). The level of facilitation was only measured on a subset of 70 locations.

Binarization of the images Each image was transformed to identify vegetated *versus* bare soil areas by performing a K-mean classification to partition the pixels in clusters of luminance intensity (using a monochromatic gray version of the image). The number of

clusters was chosen to match the vegetation cover as measured in the field ((Berdugo et al., 2017) for details). From this K-means approach, a binary landscape of the presence and absence of vegetation was obtained. In the following, each binarized vegetation landscapes of $N \times N$ pixels is denoted $Y_l^{obs} \in \{0,1\}^{N \times N}$, for $l = 1, \ldots, L$ (with $L = 345$ being the total number of landscapes).

Model of vegetation dynamics

In order to study the behavior of the observed ecosystems, we assume that each image of landscape Y_l^{obs} is the realization of a minimal model of vegetation dynamics at its asymptotic state. In this part, we drop the l index, since each landscape is treated separately. The model is referred hereafter as the model (for vegetation dynamics minimal model).

Minimal model overview The model aims at mimicking stressed ecosystems such as drylands or salt marshes: in these ecosystems, some stress-tolerant plants facilitate their local environment by increasing water infiltration, providing shading, and increasing the availability of local nutrients (Choler et al., 2001; Liancourt et al., 2005; Flores & Jurado, 2003; He et al., 2012; Qi et al., 2018). This mechanism leads to the aggregation of plants into patches separated by open bare soil areas (two-phase mosaic) (Aguiar & Sala, 1999; Scanlon et al., 2007).

The model is a stochastic cellular automaton that describes the temporal evolution of a landscape composed of $C \times C$ ($C = 100$) cells that can be in two possible states: either colonized by vegetation (V) or empty (E). Each cell is assumed to correspond to the spatial scale of an individual plant (typically in drylands between $0.25m^2$ and $1m^2$). At each time-step, the state of the cells in the landscape changes according to two probability parameters: p the local reproduction of vegetation, and q a spatial aggregation parameter that drives the spatial self-organization ((Eby et al., 2017; Sankaran et al., 2019); Fig. S12).

Note that many other models generate similar spatial structures (*e.g.,* (Kubo et al., 1996; Guichard et al., 2003; Kéfi et al., 2007b; Manor & Shnerb, 2008; Kéfi et al., 2011; Schneider & Kéfi, 2016; Génin et al., 2018b)), because the model we use belongs to a general class of models where entities (whether it is vegetation, mussels, or people) tend to aggregate in space. Nevertheless, most models are not identifiable, meaning that different parameter sets can lead to similar spatial structure distributions. Our choice of this minimal model was therefore based on the identifiability of this model from static observations (see "Parameter inference by Approximate Bayesian Computing" section), in addition to its ability to generate realistic spatial structures.

Microscopic rules The sequence of events corresponding to a time-step (from t to $t+1$) is illustrated in Fig. S13. Formally, let $I_i^t \in \{V, E\}$ be the state of the cell i at time-step t, let $\mathbf{v}(i)$ denote the four nearest neighbors of the cell i.

Starting from a landscape in state $(I_i^t)_{i\geq 1}$ at time t and defining a random sequence of the vegetated cells in the landscapes, iteration $t+1$ corresponds to the following procedure applied on all the vegetated cells in the landscape, i.e. $\{i, |I_i^t = V\}$.

1. Let i be the index of one vegetated cell in the landscape ($I_i^t = V$), referred hereafter as the focal cell (crossed cell in Fig. S13)

2. Let i' be a randomly chosen cell among the neighbors of the focal cell i ($i' \sim U\{\mathbf{v}(i)\}$, where $\mathbf{v}$ are the neighbors of the cell i and U is the uniform distribution).

   - If the cell i' is empty ($I_{i'}^t = E$, top row in Fig. S13), then either
     - it becomes colonized by vegetation with a probability p: $I_{i'}^{t+1} = V$
     - or the recruitment fails, and the focal cell dies with a probability $1-p$: $I_i^{t+1} = E$.
   - If the cell i' is vegetated ($I_{i'}^t = V$, bottom row in Fig. S13), then

- either a random cell in the neighborhood of the pair $\mathbf{v}(i, i')$ becomes vegetated with a probability q (facilitation event, $I^{t+1}_{\mathcal{U}\{\mathbf{v}(i,i')\}} = V$)
- or the focal cell dies with a probability $1 - q$ leading to $I^{t+1}_i = E$.

- Return to step 1 by considering the following vegetated state.

We ran simulations during a transient period of 1500 iterations, starting from a landscape of size $C \times C$ with high initial cover (randomly taking 80% of the cells colonized by vegetation). The 1500 time-steps transient period was enough to reach for the asymptotic convergence of all simulations done (preliminary analyses).

Modeling the scale of observation As said before, the model in defined at the scale of the individual plant, and therefore a vegetated cell corresponds to one plant. However, the pixel of the images are at a much finer spatial scale, thereby creating a mismatch of scales between the model and observed vegetation landscapes (see Fig. S14 for illustration). When willing to characterize the spatial structure from an image, the used spatial statistics might be highly correlated to the spatial resolution (Turner et al., 1989; Wiens, 1989; O'Neill et al., 1996; Wu, 2004): as an example, Fig. S15 illustrates the fact that increasing the spatial resolution of observations keeps the cover and patch-size distribution unchanged but artificially modifies other statistics such as the spatial autocorrelation or the spatial variance.

To account for this mismatch of scales between the model and the observations, we added an observation layer $\mathcal{O}$ to the model. This layer implies one parameter η representing the scale of observation of a vegetation landscape generated from the model. Practically, to account for this scale of observation, any cell of a realization of the model is replaced with a square of size $\eta \times \eta$ cells with the same type of pixel (vegetated or empty). Together with the scale layer, the has now 3 parameters ($\theta = (p, q, \eta)$) which have to be estimated.

Parameter inference by Approximate Bayesian Computing

The principal of ABC The definition of the model combined with the scale layer makes the likelihood intractable. Approximate Bayesian Computing (ABC) has proved to be a convenient method for Bayesian parameter estimation when the model is easily simulated but has non-explicit likelihood (Beaumont et al., 2002; Marjoram et al., 2003; Hartig et al., 2011, 2014).

The principle of the ABC, illustrated in Fig. 1, is to generate a set of parameters $(\theta^{(m)}) = (p^{(m)}, q^{(m)}, \eta^{(m)})$ under the prior distribution ($\theta \sim \pi$). For each parameter $\theta^{(m)}$, a vegetation landscape $Y^{(m)}$ is simulated under the model specified by the parameter $\theta^{(m)}$. If the simulated landscape $Y^{(m)}$ is "too different" from the observed landscape Y^{obs}, then the parameter $\theta^{(m)}$ is rejected, otherwise it is accepted. The landscapes are compared through a discrepancy $D(Y^{(m)}, Y^{obs})$ defined in Equation (S1) and based on summary spatial statistics. The ABC thus produces a set of accepted parameters $(\theta^{(m)*})$ which will form a sample from an approximation of the posterior distribution

Note that we could have considered Monte Carlo Markov Chains methods, Sequential Monte Carlo, or parametric likelihood estimation (using an approximated version of the likelihood) that have also been proposed for parameter inference in spatial contexts (Hartig et al., 2011, 2014). But the ABC method enables to decrease the computational cost of inference by using the same set of simulations for the inference of all images ($n = 345$; (Sirén et al., 2018)).

Priors The Bayesian inference relies on a prior distribution on the unknown parameters, namely (p, q, η). p and q are probabilities, we chose an empirical prior distribution ensuring that the resulting vegetation cover lies in $[0.05, 0.9]$ (see the corresponding prior distribution of p and q in Fig. S16). The scale parameter η was sampled from a uniform prior distribution: $\eta \sim \mathcal{U}_{\{1,\ldots,5\}}$. The range for η was chosen following the result of a principal component analysis comparing observed vegetation landscapes with the

simulated ones from the prior (Fig. S17). We sampled M = 367500 parameter sets.

Choice of the discrepancy between observations and simulations The difficulty of the ABC relies on the choice of a similarity between the simulated and the observed vegetation landscapes. We build a discrepancy based on 11 spatial summary statistics summarizing the complexity of the spatial structure. The spatial statistics are the following ones:

- First, we computed the vegetation cover (S_1) (fraction of vegetated sites), S_2 the average number of plants in the neighborhood of each vegetation site (four nearest neighbors *i.e.* von Neumann neighborhood), as well as S_3, the log-transformed vegetation clustering (average number of neighbors divided by the vegetation cover).

- In addition, we used four summary statistics used to capture the level of vegetation aggregation: namely S_4 the spatial variance, S_5 the spatial skewness, S_6 the near-neighbor correlation (Moran I), and finally S_7 the log-transformed spectral density ratio (SDR; see (Kéfi et al., 2014) for details). S_7 estimates the relative importance of long-range spatial variations compared to the total ones. We also computed S_4 the spatial variance and S_5 spatial skewness following (Sankaran et al., 2018). These metrics were computed from the R-package **spatialwarnings** (v3.0.3 ; (Génin et al., 2018a)).

- Finally, we computed four indicators from the patch-size distribution (PSD). S_8 is the power-law range (*i.e.,* the fraction of the distribution of patch sizes fitting a power law (Berdugo et al., 2017)), and the exponent of the power-law or truncated power-law which best fitted the patch size distribution. If an exponential law was the best fit for the PSD, we set the exponent value of the landscape to NA. In addition, we computed S_{10} the log-transformed fraction of the landscape covered by the largest patch (size biggest patch /total number of sites), as well as S_{11} the coefficient of variation of the patch size distribution. The latter allows accounting for the potential differences

of heterogeneity in patch-size distribution between the model and the observed vegetation landscapes. We computed S_8 to S_{11} using the functions *patchdistr_sews* and *raw_plrange*.

Note that, as illustrated in Fig. S18, these metrics are invariant with respect to the landscape size. Moreover, spatial statistics related to the patch-size distribution (S_8 to S_{11}) are invariant with respect to the spatial resolution of the vegetation landscape (Fig. S15). These summary statistics are logically correlated, as illustrated in Fig. S19, but we claim that all of them brings important information to characterize the spatial structure of the landscape. When using ABC, we cannot ensure that different sets of spatial statistics would not increase the accuracy of our inference approach (Marjoram et al., 2003). Nevertheless, we made sure that spatial statistics were sufficient by *(i)* validating the identifiability of the model parameters (p, q, η) using simulated landscapes (below), and *(ii)* tested the robustness of the ABC method to different subsets of the spatial statistics used (see Fig. S20). We give in Fig. S21 the density of spatial statistics for simulations and observations.

To build a global discrepancy between observed and simulated landscapes taking into account the 11 spatial statistics, we first Box-Cox transformed and normalized them to be able to combine them, following (Sirén et al., 2018). The obtained statistics are hereafter denoted s_k.

Finally, the discrepancy between observed and simulated vegetation landscapes is the Euclidean distance between the respective summary statistics:

$$D((s_1^{obs}, \ldots, s_m^{obs}), (s_1^{(m)}, \ldots, s_m^{sim})) = \sqrt{\sum_{k=1}^{m} (s_k^{obs} - s_k^{sim})^2} \tag{S1}$$

We followed the two-stage procedure proposed by (Sirén et al., 2018) to select the 100 parameters, leading to the closest simulations. This is roughly similar to the fraction of simulations kept in (Jabot & Chave, 2009) and a good trade-off between number of accepted simulations and the bias of the posterior parameter distributions (Fig. S22).

Note that we have considered post-sampling methods to reduce the bias of the posterior distribution (Beaumont et al., 2002; Blum & François, 2010; Li & Fearnhead, 2018). Post-sampling regression methods performed well on simulations, but none of them produced improvements on all the landscapes from the real dataset (as assessed by posterior predictive checks), so we kept the simple rejection algorithm without post-sampling regression. All the parameter inference by ABC was performed using the *abc* function from the **abc** R-package ((Csilléry et al., 2012), v2.2.1).

Illustration of the robustness of the inference method using simulated data We investigated the robustness of our inference approach using simulated landscapes for which parameters are known ("virtual landscapes"). We tested the ability of ABC to retrieve the parameters of 100 virtual landscapes (each landscape corresponding to a randomly chosen parameter (p_l, q_l)). For each landscape l, we simulated 5 scales of observation leading to $L = 500$ virtual landscapes, whose parameters were inferred by the previously described ABC procedure. We denote $(\theta_l^{(m)})_{m=1,\ldots,100}$ the posterior sample for landscape l. For each parameter p, q and η, we computed the so-called root mean-squared error (RMSE):

$$RMSE(p_l) = \sqrt{\frac{1}{100}\sum_{m=1}^{100} |p_l^{(m)} - p_l|^2} \tag{S2}$$

We normalized this metric by the RMSE computed under the prior distribution (NRMSE):

$$\text{NRMSE} = \frac{RMSE(p_l)}{\text{RMSE}_{\text{prior}}} \tag{S3}$$

A NRMSE close to zero corresponds to a posterior distribution concentrated around the true parameters p_l, while when it approaches one, the posterior distribution has not been updated using the data ($\theta^* \sim \pi$). The same formula was used with q and η instead of p.

This analysis shows that we are able to infer parameters of simulated landscapes with high accuracy (mean NRMSE $= 0.21$ for p, mean NRMSE $= 0.17$ for q and mean NRMSE

$= 0.005$ for η; Fig. S23). This high accuracy of inference for p and q is observed no matter the parameter η. In addition, we show that accounting for the scale of observation does not change the parameter that we infer for each virtual landscape (Fig. S24). Indeed, on average, we observe that the median of the posterior distribution of these 100 simulated vegetation landscapes is similar across all scales of observation (η). This analysis therefore shows that *(i)* the scale layer does not compromise the identifiability of the parameters, and that *(ii)* the parameter we infer for each site only depends on the spatial structure of the vegetation but not on the spatial resolution with which an image is characterized. All in all, this entails we can apply the ABC method to all observed vegetation landscapes **independently** of their spatial resolution.

Detection of outlier images Having validated the inference method, we performed ABC on the 345 vegetation landscapes from the global dryland dataset and estimated the posterior distribution of θ for each vegetation landscape (see as an example, posterior densities of two sites in Fig. S25 and comparison between observed and simulated landscapes from the posterior distribution of four sites in Fig. S26) We noticed that the minimal model covered well the observation but lacked of spatial heterogeneity compared to the observed landscapes (see Fig. S27 for comparison of spatial statistics between observations and accepted simulations). Interestingly, for some sites, we found a bimodality in the posterior parameters reflecting the existence of contrasting scales in the image (*e.g.,* two types of vegetation) (see the example given in Fig. S28). The model does not account for such structures. We therefore systematically detected these landscapes by testing for bimodality in the posterior distribution of parameters. Specifically, we fitted a Gaussian mixture to the posterior distributions of each site, and we removed the sites for which the bimodality of p or q was significant (*p-value* ≤ 0.05 for Hartigan's dip test; $n = 52$). This reduced the number of observed landscapes to 293. We performed this step using the function *dip.test* from the R-package **diptest** (v0.76.0).

Quantifying the resilience and the vulnerability of sites

Bifurcation diagrams For the 293 retained observed landscapes, we used the posterior distribution of parameters to predict how will the spatial structure change under a sustained increase in the level of abiotic stress each site experiences. To do so, we assumed that an increase in abiotic stress, such as aridity in our case (*e.g.*, (Huang et al., 2016; Burrell et al., 2020)), decreases the parameter linked to plant reproduction (p). This choice was motivated by the fact that *(i)* the strength of plant facilitation is expected to increase with increasing aridity (stress-gradient hypothesis, (He et al., 2013)) and *(ii)* that decreasing q would not allow to push all sites to a desert state, some would remain with a positive cover despite $q = 0$ ($n = 81$). Nevertheless, preliminary analysis made by comparing the distance to the tipping point (as defined below) with decreasing q or p showed a high correlation (Pearson correlation = 0.94, p-value < 0.001; n=212).

Thereby, for each landscape l and sample $\theta^*_{l,i}$ from the posterior distribution θ^*, we decreased $p^*_{est,l,i}$ with fixed steps (0.005) until we reached the tipping point, hereafter referred to as the desertification point ($p_{\text{crit,l,i}}$), which is the maximal value of the parameter p for which there is still vegetation. This gave 100 bifurcation diagrams (vegetation cover against parameter p) per landscape l.

Quantifying site resilience We quantified the absolute distance to the desertification point from bifurcation diagram i of landscape l, $Dist_{l,i}$ in Fig. 1, as:

$$Dist_{l,i} = p^*_{est,l,i} - p_{\text{crit,l,i}}. \tag{S4}$$

We also computed the relative distance to the desertification point $Dist_{R,l,i}$ as:

$$Dist_{R,l,i} = \frac{Dist_{l,i}}{p_{\text{crit,l,i}}}. \tag{S5}$$

This gave a sample of 100 distances to the desertification point for each landscape.

Validating our approach using other models

We validated our approach by comparing the predictions made by the inference with other models generating self-organized patterns and for which the distance to the desertification point can also be computed. We tested two models generating self-organized patterns and desertification point dynamics despite different microscopic rules compared to the minimal VDmin model. First we used a dryland vegetation model that describes with more details the life-history traits and dynamics of plants in a landscape (*e.g.*, dispersal, competition, recruitment, mortality; (Kéfi et al., 2007b)). This model allows validating the use of a minimal model that replicates well the dynamics of more complex models. In addition, to emphasize the generality of the approach when applied to vegetation landscapes with irregular patch-size distribution, we used a spatial model of mussel-beds dynamics (Guichard et al., 2003). Importantly, we could have used more models, but because both models belongs to the same universality class of models that, despite relying on different microscopic rules, generate similar types of irregular spatial structure (Pascual & Guichard, 2005; Solé, 2007; Kéfi et al., 2011), we restrict our analyses to these two. We give more information about these two models below (see Fig. 2 for model illustration).

Model of dryland vegetation dynamics with life-history traits The first model is a spatial model of vegetation dynamics in drylands that has 7 parameters describing the life history of plants in arid ecosystems ((Kéfi et al., 2007b) ; Fig. 2). Each site in the landscape can be in one of three states: degraded (D), empty but fertile (F), or colonized by vegetation (V). Vegetation produces seeds that are dispersed both locally in the four nearest-neighbors (with a fraction δ) and across the whole landscape (with a fraction $1-\delta$). Seeds can only germinate on a fertile site. Let ρ_V the fraction of sites covered by vegetation and $q_{V|F}$ the local fraction of vegetated sites in the neighborhood of a fertile site (4 nearest

neighbors), then the probability of seed recruitment is given by:

$$P(F \to V) = ((1-\delta) \times q_{V|F} + \delta\rho_V)(b - c \times \rho_V), \tag{S6}$$

where b is the recruitment probability of seeds, and c is the density-dependent competition for water. Once colonized a fertile site, the vegetation can die with a mortality rate m

$$P(V \to F) = m. \tag{S7}$$

The regeneration of a degraded site occurs at a basal rate r and is increased if neighboring sites are vegetated (*i.e.,* facilitation):

$$P(D \to F) = r + f q_{V|D}, \tag{S8}$$

where f is the strength of facilitation, and $q_{V|D}$ is the local fraction of vegetated sites in the neighborhood of a degraded site. Last, the degradation of a fertile site occurs at a rate d:

$$P(F \to D) = d. \tag{S9}$$

We ran simulations on different parameter sets. To capture different spatial structure and vegetation cover, we varied the strength of facilitation ($f \in \{0.5, 0.75, 0.9\}$) and the recruitment probability b (20 values equally spaced between 0.4 and 0.9), and fixed other parameters ($r = 0.11, d = 0.1, m = 0.1, \delta = 0.1, c = 0.1$ following (Kéfi et al., 2007b)). The simulations were performed similarly to the main contact-process model with a 1500 time step burning period before computing the spatial statistics. We applied the inference approach on these 60 "virtual landscapes", estimated their parameter posterior distributions θ^*, and computed the distance to the tipping point. To compare with, we computed the distance to the tipping point in the Kéfi model, assuming that an increase in

aridity would decrease the recruitment rate of seedlings (b).

Model of mussel-beds dynamics Besides drylands, other systems such as mussel-beds exhibit self-organized patterns characterized by a power-law distribution of patch sizes and for which, spatial structure of mussels is a good indicator of the resilience of the system (Guichard et al., 2003; Sankaran et al., 2019). To emphasize the generality of our method, we used a second model developed by Guichard et al. (Guichard et al., 2003). In this model, each site in the landscape can be in one of three states: empty (E), colonized by mussels (M), or disturbed (D) (Fig. 2). Colonization of an empty site by mussels occurs at a rate proportional to the recruitment rate α_2.

$$P(E \rightarrow M) = \alpha_2 \tag{S10}$$

A mussel can become disturbed at a rate basal rate δ_0, that is increased by a density-dependent disturbance rate α_0 when a mussel has at least one disturbed site in its neighborhood (Fig. 2):

$$P(M \rightarrow D) = \delta_0 + \alpha_0 I_{\text{dist}} \tag{S11}$$

, with $I_{\text{dist}} = 1$ if there is at least one disturbed site in the neighborhood of a mussel site, and $I_{\text{dist}} = 0$ if not. After one time-step, each disturbed site is automatically stabilized to an empty state ($d = 1$).

$$P(D \rightarrow E) = 1 \tag{S12}$$

We ran simulations with 10 values of δ_0 equally spaced between 0.01 and 0.3, three values of $\alpha_0 (\in \{0.1, 0.2, 0.3\})$, and two of $\alpha_2 (\in \{0.6, 0.8\})$ to generate virtual landscapes with different mussel cover. Next, we used our inference approach on these "virtual landscapes", estimated the posterior distributions θ^*, and computed the distance to the

tipping point. To compare with, we computed the distance to the tipping point in the Guichard model, assuming that an increase in environmental stress would increase the disturbance rate (δ_0).

For both mussel-bed and dryland vegetation models, we quantified whether our inference approach could accurately rank sites from the closest to the farthest of their tipping point using the Spearman rank correlation. To account for the posterior predictive uncertainty, we sampled 500 times each inferred distance to the tipping point, assuming that the distance to the tipping point of each virtual landscape followed a normal law with mean and standard-deviation computed on the distribution of 100 distances to the tipping point.

Assessing the drivers of global drylands resilience

Proximate drivers We first tested how vegetation cover and the spatial structure of the vegetation were related to the desertification point. We fitted a mixed-effect model with the median of the distribution of the distance to the desertification point as a response variable, and both the spatial autocorrelation of the vegetation (Moran I) and the vegetation cover as predictors. The site was included as a random intercept. This statistical model with the two predictors was then compared to statistical models with only one of the predictors (either the vegetation cover or the spatial autocorrelation of vegetation alone) using the bootstrapped-AIC of each model.

Ultimate drivers Next, to assess the effects of the soil, climatic and vegetation attributes on drylands resilience, we divided our analyses in two parts. First, we used mixed-effects models to investigate how each predictor was related with the distance to the desertification point. Then, we explored the indirect effects of each driver on the distance to the desertification point.

To assess the drivers of drylands resilience, we fitted a linear mixed-effect model with the estimated distance to the desertification point (*Dist*) as the response variable. Let $Dist_{l,s}$ be the median of the posterior distribution of the distance to the desertification point of landscape l in site s, the model reads as follows:

$$\begin{cases} Dist_{l,s} = \beta_0 + \beta_1 \mathrm{AI}_s + \beta_2 \mathrm{Sand}_s + \beta_3 \mathrm{Cover}_{l,s} + \beta_4 \mathrm{MF}_s + \\ \qquad \gamma \cdot \mathrm{Cov.}_s + \phi_s + \epsilon_{l,s} \end{cases} \tag{S13}$$

, where β_0 is the global intercept, AI is the aridity level, Sand is the soil sand content, and MF is the multifunctionality index. We also included geographical variables (Cov.) to limit potential confounding effects; namely, the latitude, longitude (cos and sin-transformed), the slope and the elevation. The predictors were weakly correlated (see Fig. S9 for the pair correlations). The site was included as a random intercept (ϕ_s).

Before running the models, we examined the distributions of all drivers, and tested their normality. We log-transformed the distance to the desertification point to improve normality. All variables were centered and reduced. We also inspected the distribution of residuals and the model assumptions using the *mcp.fnc* function from the package **LMERConvenienceFunctions**. Last, we tested for model multicollinearity using Variance Inflation Factors, and tested the potential spatial autocorrelation in the residuals using Moran tests, but neither multicollinearity nor spatial autocorrelation were observed in the model (Table S1).

From the fitted model, we then used model partial residuals to show how each predictor influenced the distance to the desertification point (Fig. 3A-C). Also, because we only had facilitation data for 184 among the 293 landscapes (70 over 115 sites), we performed the same models while including the level of facilitation in the predictors in a separate analysis.

Fitting the model using the relative distance to the desertification point led to qualitatively similar results (Fig. S29). All models were fitted using the median of the posterior distributions of q_{est} and the distance to the tipping point. We used the *lmer* function from the **lme4** package.

Indirect effects using SEMs Next, we plugged all drivers together using structural equation modeling (SEM) to investigate the indirect effects of soil, climate and vegetation attributes on the distance to the desertification point. A SEM complements the mixed-effects models by partitioning the influences between multiple variables, and separating the indirect effects of the drivers on the distance to the desertification point. The first step of a SEM analysis is to establish an a priori model based on the known effects and relationships among the drivers of the distance to the desertification point. We designed a SEM where the distance to the desertification point is influence by proximal drivers, (the vegetation cover and the spatial autocorrelation of vegetation, Moran I) based on results of previous paragraphs, that are themselves modulated by ultimate drivers (multifunctionality, aridity). We tested for a link between aridity and multifunctionality following (Berdugo et al., 2017). We did not include facilitation in the SEM given that it was measured on a subset of all data ($n = 184$).

Before running the SEM, we examined the distributions of all drivers, log-transformed the distance to the desertification point, and centered and reduced all variables. In addition, we controlled for potential effects of geographical variables not included in the SEM by fitting the SEM on the residuals of a linear model with the distance to the desertification point as response variable and the latitude, longitude (cos and sin-transformed), the slope and the elevation as predictors.

We tested the goodness of fit of our model using the Fisher-C statistic. The model has a good fit when the associated p-value is high (*e.g.*, by convention > 0.05), which is the case here (Fig. 3). Last, we calculated the standardized total effects of aridity and

multifunctionality on the distance to the desertification point by multiplying links along the paths. All coefficients were evaluated by bootstrapped (1000 replicates; see Table S2 for the confidence intervals on path coefficients). SEM analyses were performed using the **piecewiseSEM** and the **semEff** packages. The SEM were done with the absolute distance to the desertification point, but similar results were obtained using the relative distance (results not shown).

Identifying vulnerable sites

Drylands are ongoing a drastic increase in aridity, which consequently drives the desertification of large areas (Burrell et al., 2020). Desertification is also expected at more global scale and will likely drive loss of functioning of drylands (Huang et al., 2016; Berdugo et al., 2020). To turn our theoretical approach into a tool to identify the most vulnerable dryland sites of our dataset, we related the log-transformed estimated distance to the desertification point (for visual purposes) with the predicted change in aridity of each site in the next century (from 1950 to 2100) under the IPCC' RCP 8.5 scenario that assumes a sustain increase in carbon emission from human activities. We obtained these climatic data from European Copernicus climate change service (Wouters et al., 2021). We derived the change in aridity (measured as annual evaporation divided by precipitation, monthly averaged) of each site as the mean slope of aridity change between 1950 and 2100. Since different CMIP5 models were available ($n = 9$), we average the slope obtained from the different climatic models. Then, we defined the five vulnerability-based areas in Fig. 4 using a K-means clustering approach on the space defined by the distance to the desertification point and the projected aridity change. The number of clusters were chosen for their interpretability on the 2D-space.

References

Aguiar, M. R. & Sala, O. E. (1999). Patch structure, dynamics and implications for the functioning of arid ecosystems. Trends in Ecology & Evolution, 14, 273–277.

Barbier, N., COUTERON, P., Lejoly, J., Deblauwe, V. & Dejeune, O. (2006). Self-organized vegetation patterning as a fingerprint of climate and human impact on semi-arid ecosystems. Journal of Ecology, 94, 537–547.

Battiston, S., Farmer, J. D., Flache, A., Garlaschelli, D., Haldane, A. G., Heesterbeek, H., Hommes, C., Jaeger, C., May, R. & Scheffer, M. (2016). Complexity theory and financial regulation. Science, 351, 818–819.

Beaumont, M. A., Zhang, W. & Balding, D. J. (2002). Approximate Bayesian Computation in Population Genetics. Genetics, 162, 2025–2035.

Berdugo, M., Delgado-Baquerizo, M., Soliveres, S., Hernández-Clemente, R., Zhao, Y., Gaitán, J. J., Gross, N., Saiz, H., Maire, V., Lehmann, A., Rillig, M. C., Solé, R. V. & Maestre, F. T. (2020). Global ecosystem thresholds driven by aridity. Science, 367, 787–790.

Berdugo, M., Kéfi, S., Soliveres, S. & Maestre, F. T. (2017). Plant spatial patterns identify alternative ecosystem multifunctionality states in global drylands. Nature Ecology & Evolution, 1, 0003.

Blum, M. G. B. & François, O. (2010). Non-linear regression models for Approximate Bayesian Computation. Statistics and Computing, 20, 63–73.

Boettiger, C. & Hastings, A. (2013). From patterns to predictions. Nature, 493, 157–158.

Burrell, A. L., Evans, J. P. & De Kauwe, M. G. (2020). Anthropogenic climate change has driven over 5 million km2 of drylands towards desertification. Nature Communications, 11, 3853.

Burthe, S. J., Henrys, P. A., Mackay, E. B., Spears, B. M., Campbell, R., Carvalho, L., Dudley, B., Gunn, I. D. M., Johns, D. G., Maberly, S. C., May, L., Newell, M. A., Wanless, S., Winfield, I. J., Thackeray, S. J. & Daunt, F. (2016). Do early warning indicators consistently predict nonlinear change in long-term ecological data? Journal of Applied Ecology, 53, 666–676.

Buxton, J. E., Abrams, J. F., Boulton, C. A., Barlow, N., Rangel Smith, C., Van Stroud, S., Lees, K. J. & Lenton, T. M. (2022). Quantitatively monitoring the resilience of patterned vegetation in the Sahel. Global Change Biology, 28, 571–587.

Carpenter, S. R., Cole, J. J., Pace, M. L., Batt, R., Brock, W. A., Cline, T., Coloso, J., Hodgson, J. R., Kitchell, J. F., Seekell, D. A., Smith, L. & Weidel, B. (2011). Early Warnings of Regime Shifts: A Whole-Ecosystem Experiment. Science, 332, 1079–1082.

Centeno, M. A., Callahan, P. W., Larcey, P. A. & Patterson, T. S. (2023). How worlds collapse: What history, systems, and complexity can teach us about our modern world and fragile future. Taylor & Francis. ISBN 1-00-082958-8.

Choler, P., Michalet, R., Ragan, & MR, C. (2001). Facilitation and competition on gradients in alpine plant communities. Ecology, 82, 3295–3308.

Csilléry, K., François, O. & Blum, M. G. B. (2012). abc: an R package for approximate Bayesian computation (ABC). Methods in Ecology and Evolution, 3, 475–479.

Dakos, V., Kéfi, S., Rietkerk, M., van Nes, E. H. & Scheffer, M. (2011). Slowing Down in Spatially Patterned Ecosystems at the Brink of Collapse. The American Naturalist, 177, E153–E166.

Danet, A., Schneider, F. D., Anthelme, F. & Kéfi, S. (2021). Indirect facilitation drives species composition and stability in drylands. Theoretical Ecology, 14, 189–203.

Deblauwe, V., Barbier, N., Couteron, P., Lejeune, O. & Bogaert, J. (2008). The global biogeography of semi-arid periodic vegetation patterns. Global Ecology and Biogeography, 17, 715–723.

Deblauwe, V., Couteron, P., Bogaert, J. & Barbier, N. (2012). Determinants and dynamics of banded vegetation pattern migration in arid climates. Ecological Monographs, 82, 3–21.

Eby, S., Agrawal, A., Majumder, S., Dobson, A. P. & Guttal, V. (2017). Alternative stable states and spatial indicators of critical slowing down along a spatial gradient in a savanna ecosystem. Global Ecology and Biogeography, 26, 638–649.

Flores, J. & Jurado, E. (2003). Are nurse-protégé interactions more common among plants from arid environments? Journal of Vegetation Science, 14, 911–916.

Frenette Dussault, C., Shipley, B., Meziane, D. & Hingrat, Y. (2013). Trait-based climate change predictions of plant community structure in arid steppes. Journal of Ecology, 101, 484–492.

Guichard, F., Halpin, P., Allison, G., Lubchenco, J. & Menge, B. (2003). Mussel Disturbance Dynamics: Signatures of Oceanographic Forcing from Local Interactions. The American Naturalist, 161, 889–904.

Génin, A., Majumder, S., Sankaran, S., Danet, A., Guttal, V., Schneider, F. D. & Kéfi, S. (2018a). Monitoring ecosystem degradation using spatial data and the R package spatialwarnings. Methods in Ecology and Evolution, 9, 2067–2075.

Génin, A., Majumder, S., Sankaran, S., Schneider, F. D., Danet, A., Berdugo, M., Guttal, V. & Kéfi, S. (2018b). Spatially heterogeneous stressors can alter the performance of indicators of regime shifts. Ecological Indicators, 94, 520–533.

Hartig, F., Calabrese, J. M., Reineking, B., Wiegand, T. & Huth, A. (2011). Statistical

inference for stochastic simulation models - theory and application: Inference for stochastic simulation models. Ecology Letters, 14, 816–827.

Hartig, F., Dislich, C., Wiegand, T. & Huth, A. (2014). Technical Note: Approximate Bayesian parameterization of a process-based tropical forest model. Biogeosciences, 11, 1261–1272.

Hastings, A. & Wysham, D. B. (2010). Regime shifts in ecological systems can occur with no warning. Ecology Letters, 13, 464–472.

He, Q., Bertness, M. D. & Altieri, A. H. (2013). Global shifts towards positive species interactions with increasing environmental stress. Ecology Letters, 16, 695–706.

He, Q., Cui, B., Bertness, M. D. & An, Y. (2012). Testing the importance of plant strategies on facilitation using congeners in a coastal community. Ecology, 93, 2023–2029.

Huang, J., Yu, H., Guan, X., Wang, G. & Guo, R. (2016). Accelerated dryland expansion under climate change. Nature Climate Change, 6, 166–171.

Jabot, F. & Chave, J. (2009). Inferring the parameters of the neutral theory of biodiversity using phylogenetic information and implications for tropical forests. Ecology Letters, 12, 239–248.

Koffel, T., Daufresne, T. & Klausmeier, C. A. (2021). From competition to facilitation and mutualism: a general theory of the niche. Ecological Monographs, 91, e01458.

Kubo, T., Iwasa, Y. & Furumoto, N. (1996). Forest Spatial Dynamics with Gap Expansion: Total Gap Area and Gap Size Distribution. Journal of Theoretical Biology, 180, 229–246.

Kéfi, S., Guttal, V., Brock, W. A., Carpenter, S. R., Ellison, A. M., Livina, V. N., Seekell, D. A., Scheffer, M., van Nes, E. H. & Dakos, V. (2014). Early warning signals of ecological transitions: methods for spatial patterns. PLOS ONE, 9, e92097.

Kéfi, S., Génin, A., Garcia-Mayor, A., Guirado, E., Cabral, J. S., Berdugo, M., Guerber, J., Solé, R. & Maestre, F. T. (2024). Self-organization as a mechanism of resilience in dryland ecosystems. Proceedings of the National Academy of Sciences, 121, e2305153121.

Kéfi, S., Holmgren, M. & Scheffer, M. (2016). When can positive interactions cause alternative stable states in ecosystems? Functional Ecology, 30, 88–97.

Kéfi, S., Rietkerk, M., Alados, C. L., Pueyo, Y., Papanastasis, V. P., ElAich, A. & de Ruiter, P. C. (2007a). Spatial vegetation patterns and imminent desertification in Mediterranean arid ecosystems. Nature, 449, 213–217.

Kéfi, S., Rietkerk, M., Roy, M., Franc, A., de Ruiter, P. C. & Pascual, M. (2011). Robust scaling in ecosystems and the meltdown of patch size distributions before extinction: Patch size distributions towards extinction. Ecology Letters, 14, 29–35.

Kéfi, S., Rietkerk, M., van Baalen, M. & Loreau, M. (2007b). Local facilitation, bistability and transitions in arid ecosystems. Theoretical Population Biology, 71, 367–379.

Lenton, T. M., Buxton, J. E., Armstrong McKay, D. I., Abrams, J. F., Boulton, C. A., Lees, K., Powell, T. W. R., Boers, N., Cunliffe, A. M. & Dakos, V. (2022). A resilience sensing system for the biosphere. Philosophical Transactions of the Royal Society B: Biological Sciences, 377, 20210383.

Lenton, T. M., Held, H., Kriegler, E., Hall, J. W., Lucht, W., Rahmstorf, S. & Schellnhuber, H. J. (2008). Tipping elements in the Earth's climate system. Proceedings of the National Academy of Sciences, 105, 1786–1793.

Li, W. & Fearnhead, P. (2018). Convergence of regression-adjusted approximate Bayesian computation. Biometrika, 105, 301–318.

Liancourt, P., Callaway, R. M. & Michalet, R. (2005). Stress tolerance and competitive-response ability determine the outcome of biotic interactions. Ecology, 86, 1611–1618.

Lu, X., Liang, E., Babst, F., Camarero, J. J. & Büntgen, U. (2022). Warming-induced tipping points of Arctic and alpine shrub recruitment. Proceedings of the National Academy of Sciences, 119, e2118120119.

Maestre, F. T., Quero, J. L., Gotelli, N. J., Escudero, A., Ochoa, V., Delgado-Baquerizo, M., García-Gómez, M., Bowker, M. A., Soliveres, S., Escolar, C., García-Palacios, P., Berdugo, M., Valencia, E., Gozalo, B., Gallardo, A., Aguilera, L., Arredondo, T., Blones, J., Boeken, B., Bran, D., Conceição, A. A., Cabrera, O., Chaieb, M., Derak, M., Eldridge, D. J., Espinosa, C. I., Florentino, A., Gaitán, J., Gatica, M. G., Ghiloufi, W., Gómez-González, S., Gutiérrez, J. R., Hernández, R. M., Huang, X., Huber-Sannwald, E., Jankju, M., Miriti, M., Monerris, J., Mau, R. L., Morici, E., Naseri, K., Ospina, A., Polo, V., Prina, A., Pucheta, E., Ramírez-Collantes, D. A., Romão, R., Tighe, M., Torres-Díaz, C., Val, J., Veiga, J. P., Wang, D. & Zaady, E. (2012). Plant species richness and ecosystem multifunctionality in global drylands. Science, 335, 214–218.

Majumder, S., Tamma, K., Ramaswamy, S. & Guttal, V. (2019). Inferring critical thresholds of ecosystem transitions from spatial data. Ecology, 100.

Manor, A. & Shnerb, N. M. (2008). Facilitation, competition, and vegetation patchiness: From scale free distribution to patterns. Journal of Theoretical Biology, 253, 838–842.

Marjoram, P., Molitor, J., Plagnol, V. & Tavaré, S. (2003). Markov chain Monte Carlo without likelihoods. Proceedings of the National Academy of Sciences, 100, 15324–15328.

Maxwell, P. S., Eklöf, J. S., van Katwijk, M. M., O'Brien, K. R., de la Torre-Castro, M., Boström, C., Bouma, T. J., Krause-Jensen, D., Unsworth, R. K. F., van Tussenbroek, B. I. & van der Heide, T. (2017). The fundamental role of ecological feedback mechanisms for the adaptive management of seagrass ecosystems - a review: Review of feedbacks in seagrass. Biological Reviews, 92, 1521–1538.

Miguel Berdugo, Sonia Kéfi, Santiago Soliveres codina & Fernando T. Maestre

(2017). Data from "Berdugo, M.; Kéfi, S.; Soliveres, S.; Maestre, F.T. Plant spatial patterns identify alternative ecosystem multifunctionality states in global drylands. Nature Ecology & Evolution 1: 0003. 2017. doi:10.1038/s41559-016-0003". URL https://figshare.com/articles/dataset/Data_from_Berdugo_M_K_fi_S_Soliveres_S_Maestre_F_T_Plant_spatial_patterns_identify_alternative_ecosystem_multifunctionality_states_in_global_drylands_/2751904.

Mumby, P. J., Hastings, A. & Edwards, H. J. (2007). Thresholds and the resilience of Caribbean coral reefs. Nature, 450, 98–101.

O'Neill, R. V., Hunsaker, C. T., Timmins, S. P., Jackson, B. L., Jones, K. B., Riitters, K. H. & Wickham, J. D. (1996). Scale problems in reporting landscape pattern at the regional scale. Landscape Ecology, 11, 169–180.

Pascual, M. & Guichard, F. (2005). Criticality and disturbance in spatial ecological systems. Trends in Ecology & Evolution, 20, 88–95.

Pichon, B., Gounand, I., Donnet, S. & Kéfi, S. (2024). The interplay of facilitation and competition drives the emergence of multistability in dryland plant communities. URL http://biorxiv.org/lookup/doi/10.1101/2024.01.09.573035.

Qi, M., Sun, T., Xue, S., Yang, W., Shao, D. & Martínez-López, J. (2018). Competitive ability, stress tolerance and plant interactions along stress gradients. Ecology, 99, 848–857.

Reynolds, J. F., Smith, D. M. S., Lambin, E. F., Turner, B. L., Mortimore, M., Batterbury, S. P. J., Downing, T. E., Dowlatabadi, H., Fernandez, R. J., Herrick, J. E., Huber-Sannwald, E., Jiang, H., Leemans, R., Lynam, T., Maestre, F. T., Ayarza, M. & Walker, B. (2007). Global Desertification: Building a Science for Dryland Development. Science, 316, 847–851.

Rietkerk, M., Boerlijst, M., van Langevelde, F., HilleRisLambers, R., de Koppel, J., Kumar,

L., Prins, H. & de Roos, A. (2002). Self-Organization of Vegetation in Arid Ecosystems. The American Naturalist, 160, 524–530.

Sankaran, S., Majumder, S., Kéfi, S. & Guttal, V. (2018). Implications of being discrete and spatial for detecting early warning signals of regime shifts. Ecological Indicators, 94, 503–511.

Sankaran, S., Majumder, S., Viswanathan, A. & Guttal, V. (2019). Clustering and correlations: Inferring resilience from spatial patterns in ecosystems. Methods in Ecology and Evolution, 10, 2079–2089.

Scanlon, T. M., Caylor, K. K., Levin, S. A. & Rodriguez-Iturbe, I. (2007). Positive feedbacks promote power-law clustering of Kalahari vegetation. Nature, 449, 209–212.

Scheffer, M. (2009). Critical Transitions in Nature and Society. Princeton University Press.

Scheffer, M., Bascompte, J., Brock, W. A., Brovkin, V., Carpenter, S. R., Dakos, V., Held, H., van Nes, E. H., Rietkerk, M. & Sugihara, G. (2009). Early-warning signals for critical transitions. Nature, 461, 53–59.

Schneider, F. D. & Kéfi, S. (2016). Spatially heterogeneous pressure raises risk of catastrophic shifts. Theoretical Ecology, 9, 207–217.

Sirén, J., Lens, L., Cousseau, L. & Ovaskainen, O. (2018). Assessing the dynamics of natural populations by fitting individual-based models with approximate Bayesian computation. Methods in Ecology and Evolution, 9, 1286–1295.

Soliveres, S. & Maestre, F. T. (2014). Plant–plant interactions, environmental gradients and plant diversity: A global synthesis of community-level studies. Perspectives in Plant Ecology, Evolution and Systematics, 16, 154–163.

Soliveres, S., Maestre, F. T., Bowker, M. A., Torices, R., Quero, J. L., García-Gómez, M., Cabrera, O., Cea, A. P., Coaguila, D., Eldridge, D. J., Espinosa, C. I., Hemmings,

F., Monerris, J. J., Tighe, M., Delgado-Baquerizo, M., Escolar, C., García-Palacios, P., Gozalo, B., Ochoa, V., Blones, J., Derak, M., Ghiloufi, W., Gutiérrez, J. R., Hernández, R. M. & Noumi, Z. (2014). Functional traits determine plant co-occurrence more than environment or evolutionary relatedness in global drylands. Perspectives in Plant Ecology, Evolution and Systematics, 16, 164–173.

Solé, R. (2007). Scaling laws in the drier. Nature, 449, 151–153.

Turner, M. G., O'Neill, R. V., Gardner, R. H. & Milne, B. T. (1989). Effects of changing spatial scale on the analysis of landscape pattern. Landscape Ecology, 3, 153–162.

van Belzen, J., van de Koppel, J., Kirwan, M. L., van der Wal, D., Herman, P. M. J., Dakos, V., Kéfi, S., Scheffer, M., Guntenspergen, G. R. & Bouma, T. J. (2017). Vegetation recovery in tidal marshes reveals critical slowing down under increased inundation. Nature Communications, 8, 15811.

van de Koppel, J., Gascoigne, J. C., Theraulaz, G., Rietkerk, M., Mooij, W. M. & Herman, P. M. J. (2008). Experimental Evidence for Spatial Self-Organization and Its Emergent Effects in Mussel Bed Ecosystems. Science, 322, 739–742.

Van De Leemput, I. A., Wichers, M., Cramer, A. O. J., Borsboom, D., Tuerlinckx, F., Kuppens, P., Van Nes, E. H., Viechtbauer, W., Giltay, E. J., Aggen, S. H., Derom, C., Jacobs, N., Kendler, K. S., Van Der Maas, H. L. J., Neale, M. C., Peeters, F., Thiery, E., Zachar, P. & Scheffer, M. (2014). Critical slowing down as early warning for the onset and termination of depression. Proceedings of the National Academy of Sciences, 111, 87–92.

van der Heide, T., Bouma, T. J., van Nes, E. H., van de Koppel, J., Scheffer, M., Roelofs, J. G. M., van Katwijk, M. M. & Smolders, A. J. P. (2010). Spatial self-organized patterning in seagrasses along a depth gradient of an intertidal ecosystem. Ecology, 91, 362–369.

Veraart, A. J., Faassen, E. J., Dakos, V., van Nes, E. H., Lürling, M. & Scheffer, M. (2012). Recovery rates reflect distance to a tipping point in a living system. Nature, 481, 357–359.

Wiens, J. A. (1989). Spatial Scaling in Ecology. Functional Ecology, 3, 385.

Wouters, H., Berckmans, J., Maes, R., Vanuytrecht, E. & De Ridder, K. (2021). Global bioclimatic indicators from 1950 to 2100 derived from climate projections.

Wu, J. (2004). Effects of changing scale on landscape pattern analysis: scaling relations. Landscape Ecology, 19, 125–138.

Zhang, H., Wang, Q., Zhang, W., Havlin, S. & Gao, J. (2022). Estimating comparable distances to tipping points across mutualistic systems by scaled recovery rates. Nature Ecology & Evolution, 6, 1524–1536.